Earth and Planetary Science Letters 509 (2019) 66–77

Contents lists available at ScienceDirect

Earth and Planetary Science Letters

www.elsevier.com/locate/epsl

# Weathering front under a granite ridge revealed through full-3D seismic ambient-noise tomography

Wei Wang [a,*], Po Chen [a], Ian Keifer [a], Ken Dueker [a], En-Jui Lee [b], Dawei Mu [c], Jianying Jiao [a], Ye Zhang [a], Bradley Carr [a]

[a] Department of Geology and Geophysics, University of Wyoming, USA
[b] Department of Earth Sciences, National Cheng-Kung University, Taiwan
[c] San Diego Supercomputer Center, University of California, San Diego, USA

ARTICLE INFO

*Article history:*
Received 16 May 2018
Received in revised form 26 December 2018
Accepted 30 December 2018
Available online xxxx
Editor: J.-P. Avouac

*Keywords:*
critical zone
weathering front
discontinuous Galerkin method
full-3D tomography
ambient-noise tomography

ABSTRACT

Seismic tomography, when calibrated with borehole data, can be a highly effective tool for investigating the deep structure of the critical zone. In this study, we have successfully applied seismic adjoint tomography to obtain a fully three-dimensional shear-wave velocity model under a granitic ridge in the Blair-Wallis watershed, southeastern Wyoming. The seismic data used in our tomography are ambient-noise Green's functions obtained from a minimally invasive, "large-N" seismic survey using a square array of 400 autonomous geophones. Lateral variations of our 3D shear-wave velocity model show strong correlations with surface topography. Depth variations of our velocity model may give clues about the depth interval within which chemical weathering plays a significant role. With the calibration of borehole casing depths and saprolite refusal depths, we selected the isosurface of shear-wave velocity 491 m/s as the interface between highly chemically weathered saprolite and fractured bedrocks, which we use to represent the weathering front in this study. Large-scale spatial variations of the weathering front are consistent with groundwater table, which provides observational support to a recently proposed hypothesis that subsurface weathering is mainly driven by bedrock drainage of chemically equilibrated water. Small-scale spatial variations of the weathering front calls for more sophisticated mechanisms that couple the effect of top-down infiltration of reactive meteoric water with the influence of pre-existing fractures.



## 1. Introduction

The outermost layer of the solid Earth, named the Critical Zone (CZ) (NRC, 2001) due to its essential role in sustaining terrestrial life (Brantley et al., 2006), is mainly shaped by two geological processes working in tandem: weathering, which breaks down rock through chemical, biological and mechanical processes, and erosion, which transports mass in the CZ and removes material from the land surface. As land surfaces erode, fresh bedrock rises up and enters the CZ feed-through reactor (Anderson et al., 2007), in which weathering irreversibly breaks and alters the rock, transforming it into fractured bedrock, saprolite and soil, with increasing degree of physical breakup, chemical dissolution and alteration (Anderson et al., 2007; Befus et al., 2011; Holbrook et al., 2014). The saprolite is usually defined as highly chemically weathered rock that still retains original lithic fabric of deep parent rock (Merrill, 1897; Stolt and Baker, 1994). The transition between fresh bedrock and chemically weathered rock, which can be a sharp boundary or a gradational zone, is called the weathering front, where some of the most crucial chemical and physical weathering processes occur (Anderson et al., 2007).

Mechanisms for regulating the development of the weathering front have been under intense study recently. One hypothesis suggests that downward propagation of the weathering front is primarily controlled by "top-down" processes driven mainly by infiltration and percolation of chemically reactive meteoric water, which leads to a weathering front depth determined by the balance between groundwater residence time and mineral reaction kinetics (e.g., Lebedeva and Brantley, 2013). An alternative hypothesis puts more emphasis on the control of "bottom-up" processes, proposing that drainage of uplifted bedrock, previously saturated with nearly stagnant and chemically equilibrated fluids, permits the introduction of reactive meteoric water from above and the weathering front is thereby set by the uppermost extent of

* Corresponding author.
*E-mail address:* wangxiawei0619@gmail.com (W. Wang).

https://doi.org/10.1016/j.epsl.2018.12.038
0012-821X/

undrained bedrock, which is at the groundwater table (e.g., Rempe and Dietrich, 2014).

Improved understanding of these mechanisms has so far been hampered by the difficulty in accessing the weathering front directly, especially under terrains with thick weathered zones. Drilling and coring can provide direct measurements of the deep CZ. However, they are often expensive and logistically challenging and the spot measurements obtained from a few sporadically located boreholes may not be representative of the entire area, especially in areas with strong lateral heterogeneities. Seismic tomography is minimally invasive, relatively inexpensive and provides indirect estimates of physical properties of the deep CZ over large areas quickly. Past experiences (e.g., Hunter et al., 1984; Befus et al., 2011; Holbrook et al., 2014) have shown that seismic tomography is a highly useful complement to drilling/coring in CZ studies, especially when it can be calibrated with direct measurements from boreholes. In addition, results from seismic tomography can often provide crucial guidance for selecting the most useful sites for drilling/coring and other excavation and sampling efforts.

In this letter, we report that recent advances in full-3D seismic tomography (e.g., Tarantola, 1988; Tromp et al., 2005; Chen et al., 2007; Tape et al., 2009; Fichtner, 2011; Lee et al., 2014; Chen and Lee, 2015) have opened up possibilities of imaging the weathering front under thick weathered zones through minimally invasive, full-wavefield, 2D seismic ambient-noise surveys. In particular, full-3D seismic ambient-noise tomography based upon the adjoint method has been successfully applied to image crustal and upper mantle structures (Chen et al., 2014; Gao and Shen, 2014). In this study, we show images of the weathering front under a granite ridge in the Blair-Wallis (BW) watershed obtained from full-3D seismic ambient-noise tomography. Our images suggest that the "top-down" and "bottom-up" mechanisms are not mutually exclusive, "bottom-up" processes mainly influence large-scale variations of the weathering front, while small-scale variations of the weathering front may require explanations from "top-down" processes, perhaps facilitated by fractures inherited from deep parent rocks (Novitsky et al., 2018).

## 2. Geological and hydrological settings

The BW watershed in the Laramie Range southeastern Wyoming (Fig. 1a) is a granitic terrain with a thick and heterogeneous weathered zone. The erosion rate obtained from cosmogenic $^{10}$Be in alluvium at a site ∼6 km to the northeast is 23±7 mm/kyr (Dethier et al., 2014). This area is underlain by the Sherman Batholith mainly composed of ∼1.43 Ga granitic rocks (Frost et al., 1999). The volumetrically dominant Sherman Granite commonly weathers deeply into thick grusses (i.e., coarse-grained fragments of disintegrated granite due to weathering) (Eggler et al., 1969). Distinct from the rugged topography of the Front Range, the Laramie Range in this region has remarkably flat topography, which likely resulted from thorough disintegration of Sherman granites into grusses (Eggler et al., 1969; Chapin and Kelley, 1997). Borehole drilling and augering at several isolated sites in the BW area (Fig. 1a) recovered highly friable and porous saprolite materials (grusses intermixed with corestones) (Fig. 1b) down to at least ∼9 m depth. Such a thick, porous saprolite layer can play a major role in influencing subsurface water flow and storage (Carey and Paige, 2016) and an improved understanding of the water balance for the ecosystem in this region calls for 3D characterization of the saprolite layer.

At the BW watershed, the dominant form of precipitation is snow, which amounts to ∼90% of the ∼620 mm total annual precipitation (NRCS, 2015). Snow melts from April to June, which produces easily identifiable peaks on the stream hydrographs. The ridge of our study site is located at the confluence of two valleys (Fig. 1a). The southern valley is occupied by a small perennial stream, which drains ∼4.1 km$^2$ watershed. The northern valley becomes a small wetland during peak snowmelt, but is dry most of the year. This area is located on the northwestern boundary of the High Plains Aquifer, which is one of the world's largest aquifers. Large yields of ground water in this area mainly come from the White River Formation of Oligocene, the Arikaree Formation of Miocene and the Ogallala Formation of Miocene and Pliocene. The principal source of ground water recharge is precipitation, ∼5% of which is estimated to be ground water recharge. The water table slopes gently eastward with a gradient of ∼7.6 m/km (Lowry et al., 1967).

## 3. Ambient-noise Green's functions

With the rapid advances in seismic data acquisition technology, seismic ambient-noise tomography, which maps subsurface shear-wave velocity using diffusive and continuous seismic ambient-noise sources, is emerging as an appealing alternative to conventional ballistic-wave tomography using either earthquakes or manmade point sources (e.g., Shapiro et al., 2005; Lin et al., 2008). The recent availability of cable-free, autonomous geophones has opened up the possibility of recording the full ambient-noise wavefields using large, dense 2D seismic arrays, which is sometimes called "large-N" seismic analysis. The number of autonomous geophones used in such a large-N analysis is often much larger than those used in a typical conventional ballistic-wave seismic survey. In August 2015, we carried out a large-N seismic survey by deploying a 2D array of 400 autonomous FairfieldNodal's ZLand nodes equipped with vertical-component geophones (10 Hz corner frequency) at our BW site (Fig. 1a). The geophones were distributed on a ∼190 m by ∼190 m square grid with ∼10 m grid-spacing and recorded the ambient-noise wavefields at a 500-Hz sampling rate for 4 days, producing a dataset of ∼0.25 TB.

The recorded ambient-noise data were processed following a sequence of operations known as "seismic interferometry" to obtain ∼80,000 inter-geophone ambient-noise Green's functions. In our study, we have adopted the conventional seismic interferometry technique (e.g., Bensen et al., 2007), which involves three steps carried out in sequence: (1) single-geophone processing (i.e., the seismogram recorded by each geophone was cut into 2-minute-long segments and normalized in time domain and frequency domain), (2) inter-geophone cross-correlation (i.e., for each pair of geophones in the array, we cross-correlated the normalized 2-minute-long segments of the same time span and each cross-correlation was normalized using its maximum amplitude) and (3) temporal stacking (i.e., summing all normalized cross-correlations of different time spans for each geophone pair). We carried out all calculations using an efficient parallel algorithm, pSIN (Parallel Seismic INtererometry) (Chen et al., 2016), which reduced the total amount of computing time for our BW dataset from ∼14 days on a single state-of-the-art four-core desktop computer to ∼52 min on 2112 CPU cores on the IBM iDataPlex cluster (code named "Yellowstone") at the NCAR-Wyoming Supercomputing Center.

The stacked cross-correlation for a pair of geophones is an approximation to the Green's function between the two geophones (i.e., the response of the subsurface medium recorded at one geophone as if there was an impulse excitation at the other geophone). For the BW array used in this study, the majority of noise sources come from anthropogenic activities on nearby roads and perhaps also from the small stream in the southern valley. The spatial distribution of the noise sources is inhomogeneous and to suppress the effect of uneven spatial distribution of noise sources, we calculated the average of the positive- and negative-lag portions of each cross-correlation, as suggested in Lin et al. (2008).

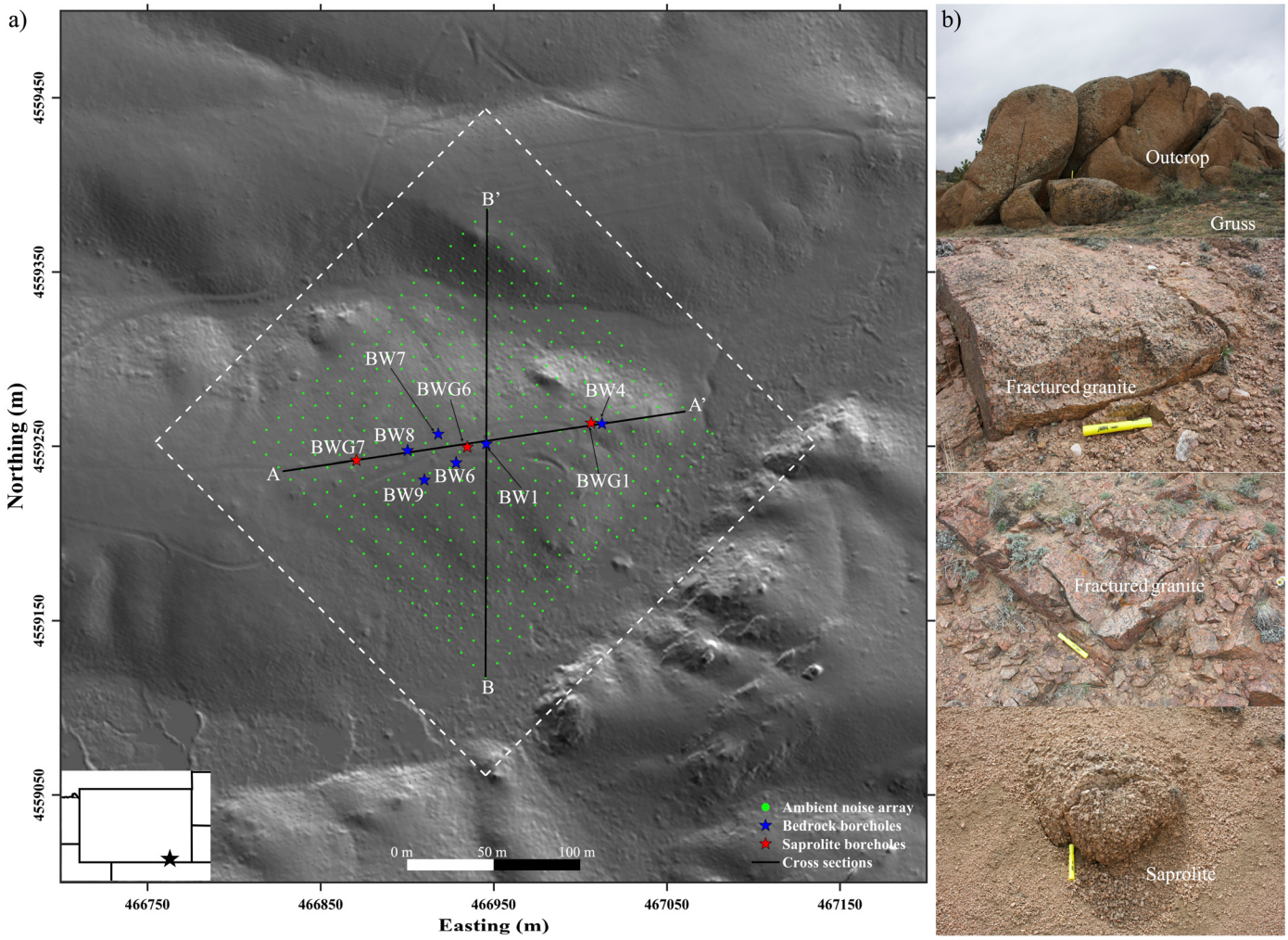


**Fig. 1.** a) Map and location of Blair Wallis watershed, Laramie Range, Wyoming. Green dots: locations of autonomous geophones. Red stars: locations of bedrock borehole. Blue stars: saprolite boreholes. White dashed box: boundary for tomography. Black lines: locations of two cross sections as shown in Fig. 8. b) Field photos of outcrops and fractured rocks at research site. (For interpretation of the colors in the figure(s), the reader is referred to the web version of this article.)

Examples of our averaged causal ambient-noise Green's functions obtained from the BW array are shown in Fig. 2a. While the corner frequency of our geophones is at 10 Hz, we observed emergence of coherent signals between 3 and 30 Hz (Fig. 2b). After experimenting with a number of band-pass filters of different corner frequencies, we found that the fundamental-mode Rayleigh wave, which were used in our tomographic inversion, has the highest signal-to-noise ratio between 12 and 30 Hz and an average speed of ∼342 m/s (Fig. 2c). In addition to the fundamental-mode Rayleigh wave that can be traced across the entire array, a very weak, slower arrival (∼180 m/s) appears across short inter-geophone distances (Fig. 2), which may suggest the existence of a much slower layer in the uppermost few meters.

## 4. Methods

Rapid advances in high-performance computing technology in the past few decades have recently enabled the application of fully three-dimensional tomography (F3DT), in which the starting model can be 3D in space and the Fréchet (sensitivity) kernels are computed using the full physics of 3D wave propagation by numerically solving the elastodynamic equations. F3DT can employ any types of seismological observables, including frequency-dependent group delays of ambient-noise Green's functions. The nonlinearity of tomographic inversion is fully accounted for in F3DT through iterations.

### 4.1. Numerical solver

In this study, we adopted the discontinuous-Galerkin method (DGM) as our numerical solver of the elastodynamic equations. Like the spectral-element method (SEM), the solution inside each element is approximated using a set of orthogonal basis functions, which leads to high-order spatial accuracy and diagonal mass matrices. Different from the SEM, the solution is allowed to be discontinuous across element boundaries and the discontinuities are treated using well-established ideas of numerical flux functions from high-order finite-volume framework. The DGM was introduced to solve 2D isotropic elastic wave equation in Käser and Dumbser (2006) and extended to 3D isotropic case in Dumbser and Käser (2006). Additional developments, extensions and applications of the DGM were documented in Käser et al. (2010) and references therein.

An advantage of the DGM is its capability to achieve high-order accuracy on unstructured tetrahedral meshes. Fig. 3 shows an example of the tetrahedral mesh used in our 3D wave-propagation simulations in the BW area. The mesh conforms to surface topography, which was provided from a LiDAR survey of the area and has a spatial resolution of ∼0.5 m. The modeling volume is 270 m by

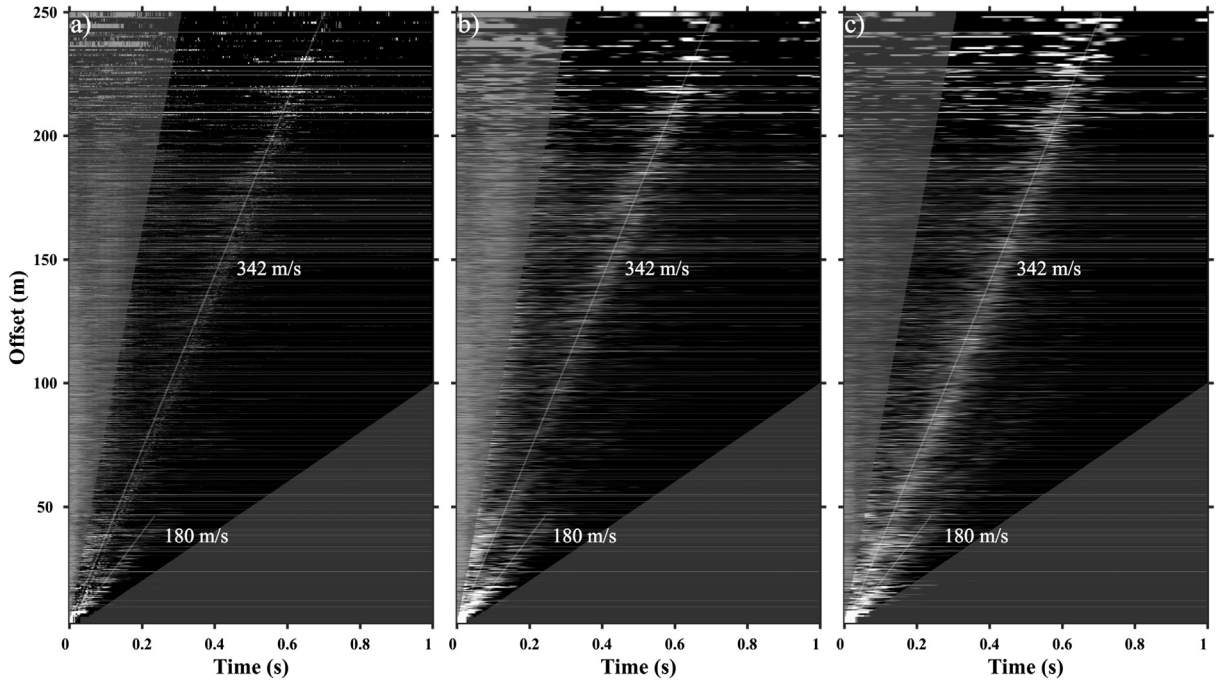


**Fig. 2.** a) Amplitudes of envelopes of stacked, causal ambient-noise Green's functions; b) Amplitudes of envelopes obtained after filtering the ambient noise Green's functions with a 4th order Butterworth bandpass filter with corner frequencies at 3 Hz and 30 Hz. c) Amplitudes of envelopes obtained after filtering ambient noise Green's functions with a 4th order Butterworth bandpass filter with corner frequencies at 12 Hz and 30 Hz.

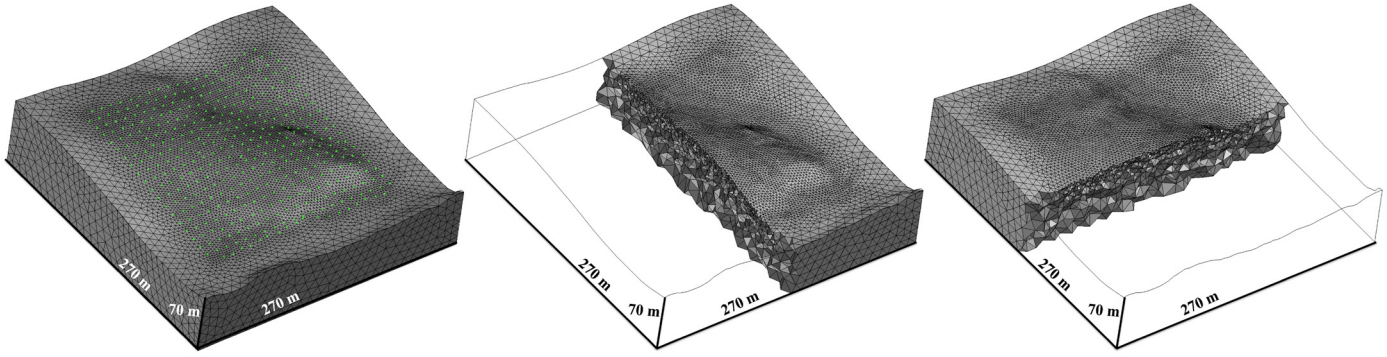


**Fig. 3.** Perspective views of the tetrahedral mesh used in our DG simulations. The top surface of the mesh conforms to local topography derived from LiDAR data. Locations of the autonomous geophones are indicated using green dots. Element sizes increase gradually with both depth and the distance from the seismic array.

270 m in the two horizontal dimensions and 70 m in the vertical dimension, with the BW seismic array located in the center of the free surface. The element sizes are adapted to the seismic velocity model, which increases with depth. The cut-away views in Fig. 3 show that element sizes increase from ∼2 m at shallow depths to ∼10 m at the bottom of the mesh, such that the number of elements per shortest wavelength is roughly the same throughout the modeling volume. In the two lateral dimensions, element sizes are generally smaller under the BW seismic array and slightly larger outside the seismic array. These mesh refinements in both vertical and lateral dimensions allow us to minimize computational cost while retaining numerical accuracy.

### 4.2. Frequency-dependent group delays

Model-predicted (i.e., synthetic) Green's functions were computed using the DGM for the reference seismic velocity model by assuming a vertical, spatially and temporally Dirac virtual source located at one of the geophones. Fig. 4a shows an example of the synthetic Rayleigh wave and the observed Rayleigh wave obtained by windowing the complete synthetic Green's function and the corresponding ambient-noise Green's function using a cosine-taper window. Frequency-dependent phase and amplitude differences between the synthetic and observed Rayleigh waves can be obtained using the technique of Holschneider et al. (2005). In particular, the frequency-domain phase and amplitude misfits can be represented as weighted summations of B-spline functions and the optimal weights can be found by minimizing the energy of the time-domain waveform differences using the Levenberg–Marquardt algorithm (Fig. 4b; Holschneider et al., 2005). Frequency-dependent group delays between observed and synthetic Rayleigh waves (Fig. 4d) can then be computed from the phase difference within a frequency band of sufficiently high signal-to-noise ratios (Fig. 4c). We adopted the Geophysical Wavelet Library (Kulesh et al., 2008) for obtaining the misfit measurements.

Among the ∼80,000 ambient-noise Green's functions (Fig. 2) we selected 5676 with the highest signal-to-noise ratios. This selected subset of ambient-noise Green's functions provide a dense and fairly even coverage throughout the entire modeling area. For each ambient-noise Green's function, we measured frequency-dependent group delays from 10 to 32 Hz with a 0.5 Hz interval,

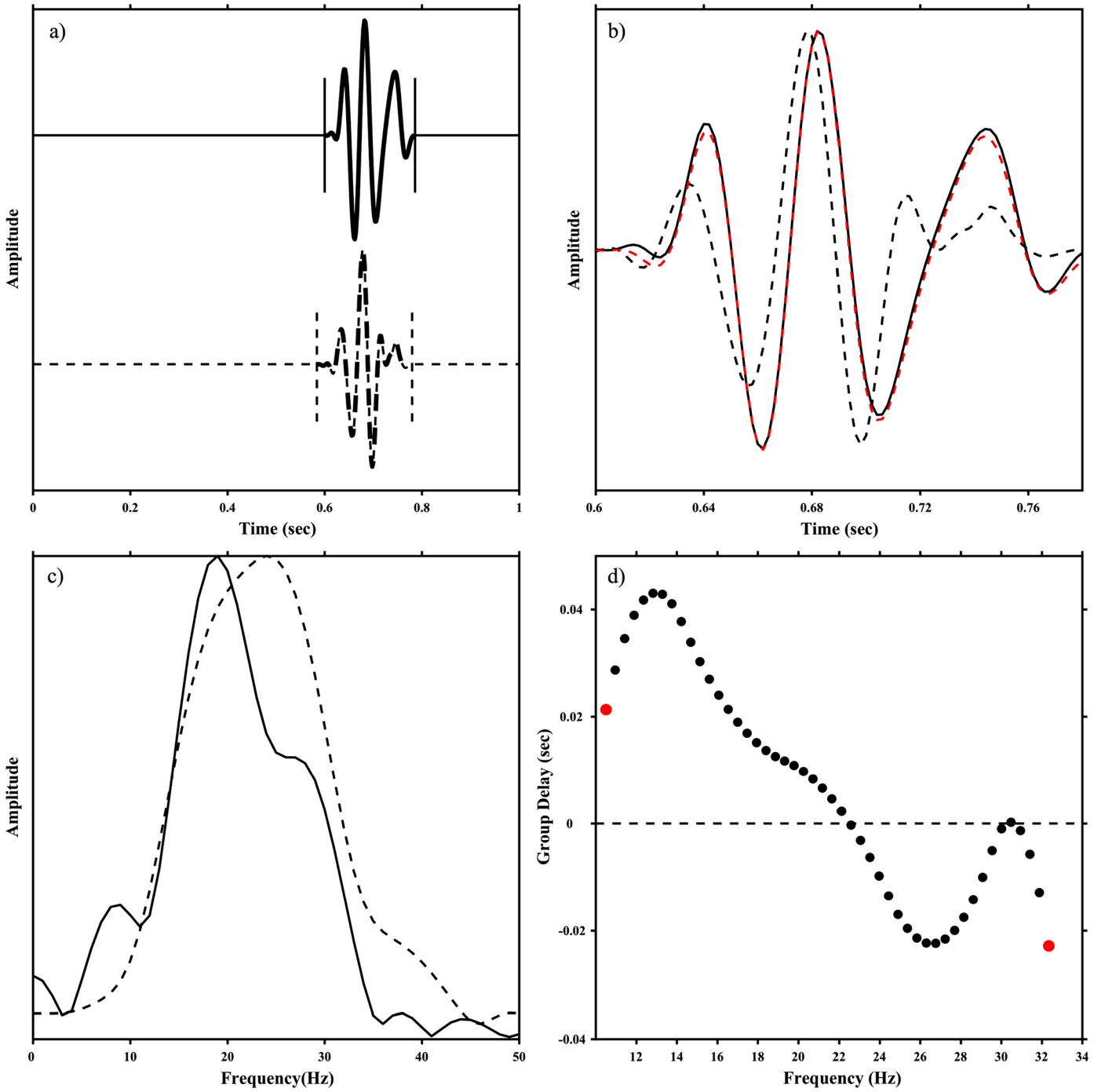


**Fig. 4.** a) An example of the Rayleigh wave on the ambient-noise Green's function (solid line) and the Rayleigh wave on the corresponding synthetic seismogram (dash line). Vertical lines: the boundaries of the tapered windows for isolating the Rayleigh waves; b) solid line: observed waveform, black dash line: the synthetic waveform, red dash line: the synthetic waveform after applying the optimized phase and amplitude corrections; c) amplitude spectrums of the observed (solid line) and synthetic (dashed) waveforms; d) Frequency-dependent group delays between observed and synthetic waveforms. Adjoint kernels for the two red measurements are shown in Fig. 5.

resulting in ~200,000 measurements for the entire subset. We then minimized the objective function defined as the sum of the squares of the group delays using the conjugate-gradient algorithm (Press et al., 1992).

### 4.3. Adjoint kernels

The gradient of the objective function with respect to the shear-wave velocity in each element of our mesh can be computed using the adjoint-wavefield method, which involves back-propagating the group-delays from the receivers using the numerical solver of the 3D elastodynamic equation to construct the adjoint wavefield (Tarantola, 1988; Tromp et al., 2005). The zero-lag temporal correlation between the forward wavefield from the virtual Dirac source and the corresponding adjoint wavefield is sometimes called the adjoint kernel (Tarantola, 1988; Tromp et al., 2005).

Fig. 5 shows examples of adjoint kernels used in our inversion. At 10 Hz, the group delay is positive (Fig. 4d), i.e., the observed wave arrives at the receiver later than model prediction, and the adjoint kernel at this frequency is mostly negative (Fig. 5b), indicating that the reference shear-wave velocity is too fast in the kernel's domain. At 32 Hz, the group delay is negative (Fig. 4d)

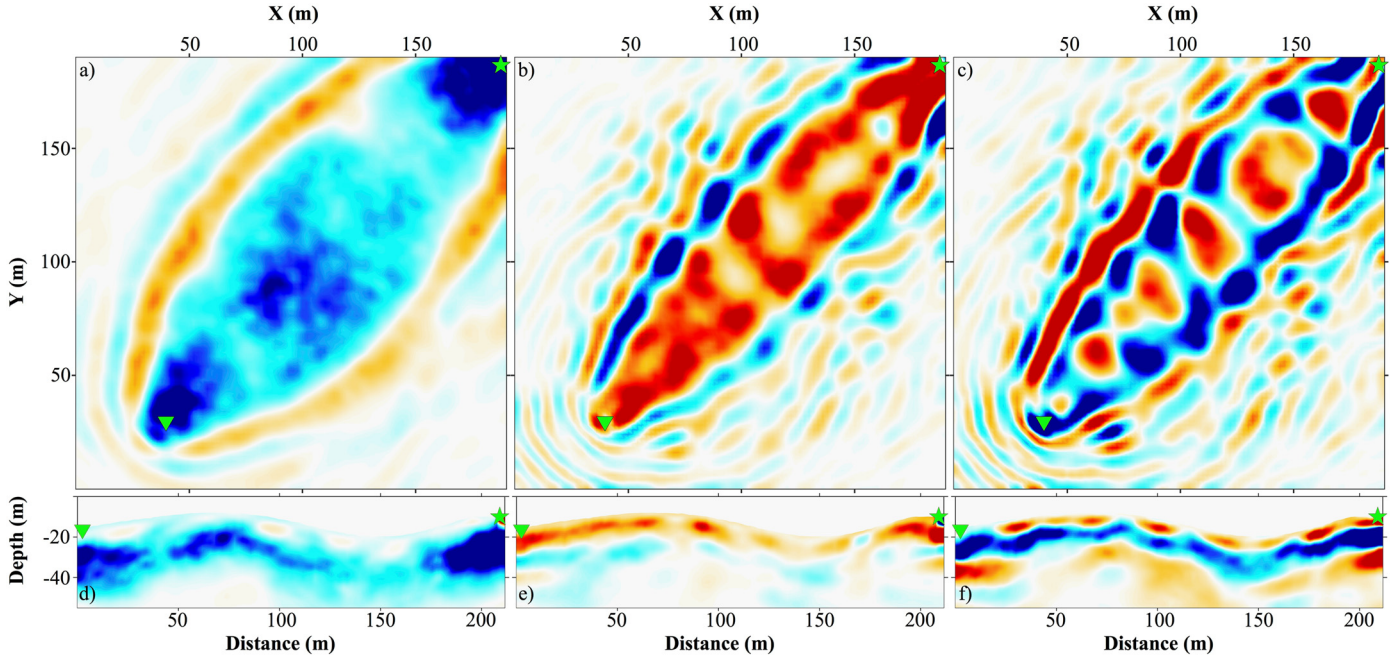


**Fig. 5.** Examples of adjoint kernels for the Rayleigh wave shown in Fig. 4. a) Map view of adjoint kernel at 15 m below free surface for group delay measured at 10 Hz; b) map view of kernel at 5 m below free surface for group delay measured at 32 Hz; c) map view of the sum of adjoint kernels at 5 m below free surface for all group delays measured from 10 Hz to 32 Hz; d)–f) cross-section views perpendicular to the source (pentagram)-receiver (triangle) plane. Warm color (red-orange): negative sensitivity, indicating an increase in shear-wave velocity will reduce the group delay; cold colors: positive sensitivity, indicating a decrease in shear-wave velocity will reduce the group delay.

and the kernel is mostly positive (Fig. 5c), indicating the reference shear-wave velocity is too slow in its domain. The gradient of the objective function is the sum of adjoint kernels over all frequencies (e.g., Fig. 5c) and over all source-receiver paths. Kernels at lower frequencies (e.g., Fig. 5b) are usually more sensitive to deeper structures than those at higher frequencies (e.g., Fig. 5c). The sum of kernels over all frequencies for the source-receiver path shown in Fig. 5a indicates that along this path the shear-wave velocity in the reference model is too slow at shallow depths and too fast at large depths (Fig. 5d).

## 5. Results and discussion

The gradient of the objective function was used for minimizing the objective function using the conjugate-gradient (CG) algorithm. In a typical CG implementation, the descent direction at the current iteration is a linear combination of the descent direction of the previous iteration and the gradient of the current iteration and we used the formula of Fletcher-Reeves (Press et al., 1992).

To initiate the iterative CG optimization, we generated a starting shear-wave velocity model that increases from 300 m/s at the free surface linearly with depth at a constant gradient of 20 m/s/m. The 1D starting model was obtained from laterally averaging 3D model of Keifer and Dueker (under review). The P-velocity was then scaled from the S-velocity by assuming a constant Poisson's ratio of 0.25 and the density was obtained from the P-velocity using the Gardner's equation.

After 5 adjoint iterations, the objective function reduced by ∼62% (Fig. 6a). The 5th iteration generated only insignificant changes to the shear-wave velocity model and we stopped iterating further. The histogram of the group delays of the starting model shows a negative bias (Fig. 6a), which indicates that on average the starting model is too slow. The updated model after the 5th adjoint iteration has corrected this bias and reduced the variance in the group delays substantially (Fig. 6a).

The Hessian of the objective function allows us to obtain estimates of our model's resolution. In Fig. 7bc, we show map views and cross-sections of checkerboard tests obtained using the Gauss–Newton approximate Hessian of the 5th iteration. To obtain the approximate Hessian, we calculated the data sensitivity kernel for every group-delay misfit measurement using the scattering-integral technique (Zhao et al., 2005; Chen et al., 2007; Lee et al., 2014) and the Gauss–Newton normal equation was solved using the scalable parallel LSQR code of Lee and Chen (2013).

The recovered checkerboard pattern (Fig. 7bc) depends upon the source-receiver paths, the particular wave arrivals used in the inversion and their data sensitivity kernels at different frequencies. The checker sizes are ∼28 m in horizontal directions and ∼5 m in the vertical direction, which are generally smaller than the structural features that we discuss and interpret in the following sections. In general, the checkerboard patterns are better recovered under areas covered by our seismic data array than areas outside of our array boundary. Close to the center of our seismic data array, where the total number of crossing source-receiver paths is the largest, the checkerboard pattern can be recovered down to 25–30 m depth below the free surface. Towards the boundary of the seismic array, the checkerboard pattern can still be recovered to about 15–20 m depth below the free surface. In general, the recovery deteriorates quickly below ∼25 m depth. The structural features we discuss in the following generally fall inside of the volume where we have satisfactory recovery of the checkerboard pattern.

### 5.1. Lateral variations in shear-wave velocity

Fig. 7a shows map-view plots of the updated shear-wave velocity model after the 5th adjoint iteration at constant depths below the free surface. In addition to various small-scale heterogeneities, the map-view plots show two clear general spatial patterns: (1) at shallow depths (∼5 m), the shear-wave velocity is lower beneath the ridge and higher under the valley and (2) between ∼10 m and ∼20 m depths the shear-wave velocity shows a distinct correlation

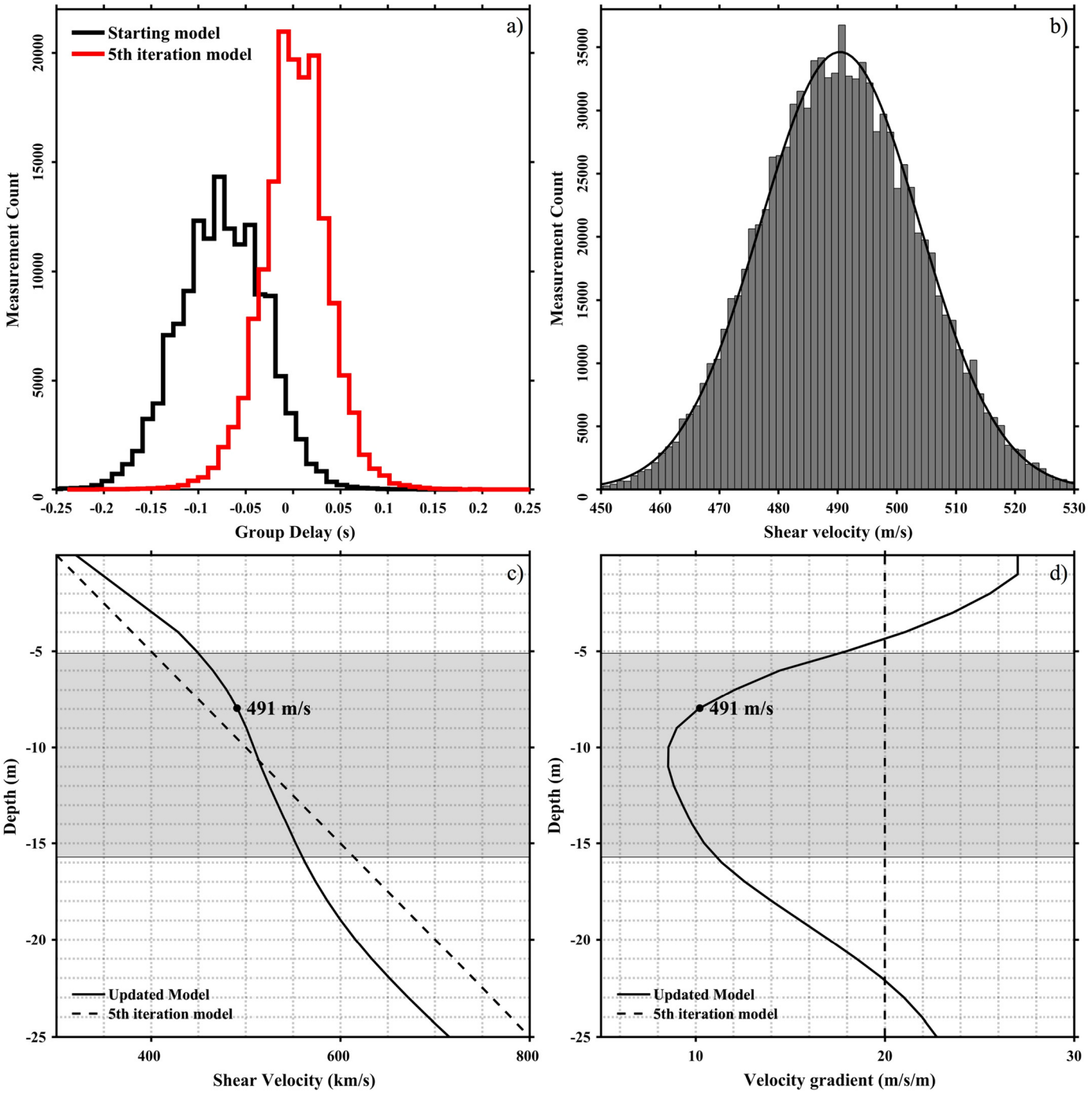


**Fig. 6.** a) Histograms of group delays for the starting model (black) and the updated model obtained after 5 adjoint iterations (red); b) histogram obtained from a bootstrap process that minimizes the misfit between the velocity isosurface and the borehole saprolite depth measurements, black solid line: the best-fit normal distribution; c) laterally averaged shear-wave velocity with as a function of depth for the 3D updated model (solid line) and the laterally homogeneous starting model (dash line); d) the derivatives with respect to depth for the velocity-depth profiles shown in c).

with topographic slope, i.e., the velocity is higher where the surface topography is steep and lower where the surface topography is gentle.

Correlations between near-surface shear-wave velocity and surface topography have been documented in previous geotechnical studies for the purpose of evaluating ground-motion amplification by surficial materials during disastrous earthquakes (e.g., Wald and Allen, 2007). In particular, topographic slope has been used as a proxy for estimating $V_{S30}$ (i.e., the average shear-wave velocity from surface to 30 m depth) based upon the hypothesis that more competent rocks, which usually have higher shear-wave velocities, are more capable of sustaining steep slopes, whereas environments with gentle slops are more likely to retain soft sediments with lower shear-wave velocities. This general hypothesis has been validated extensively using $V_{S30}$ observations in different tectonic regimes around the globe (Wald and Allen, 2007) and is practically important in seismic hazard analysis. However, it offers no direct insights into the architecture of the CZ and the processes that create and shape the CZ.

It is unlikely that lithological heterogeneities are the primary cause for the lateral variations in shear-wave velocity observed in Fig. 7a. The geochemically distinct Lincoln and porphyritic granites

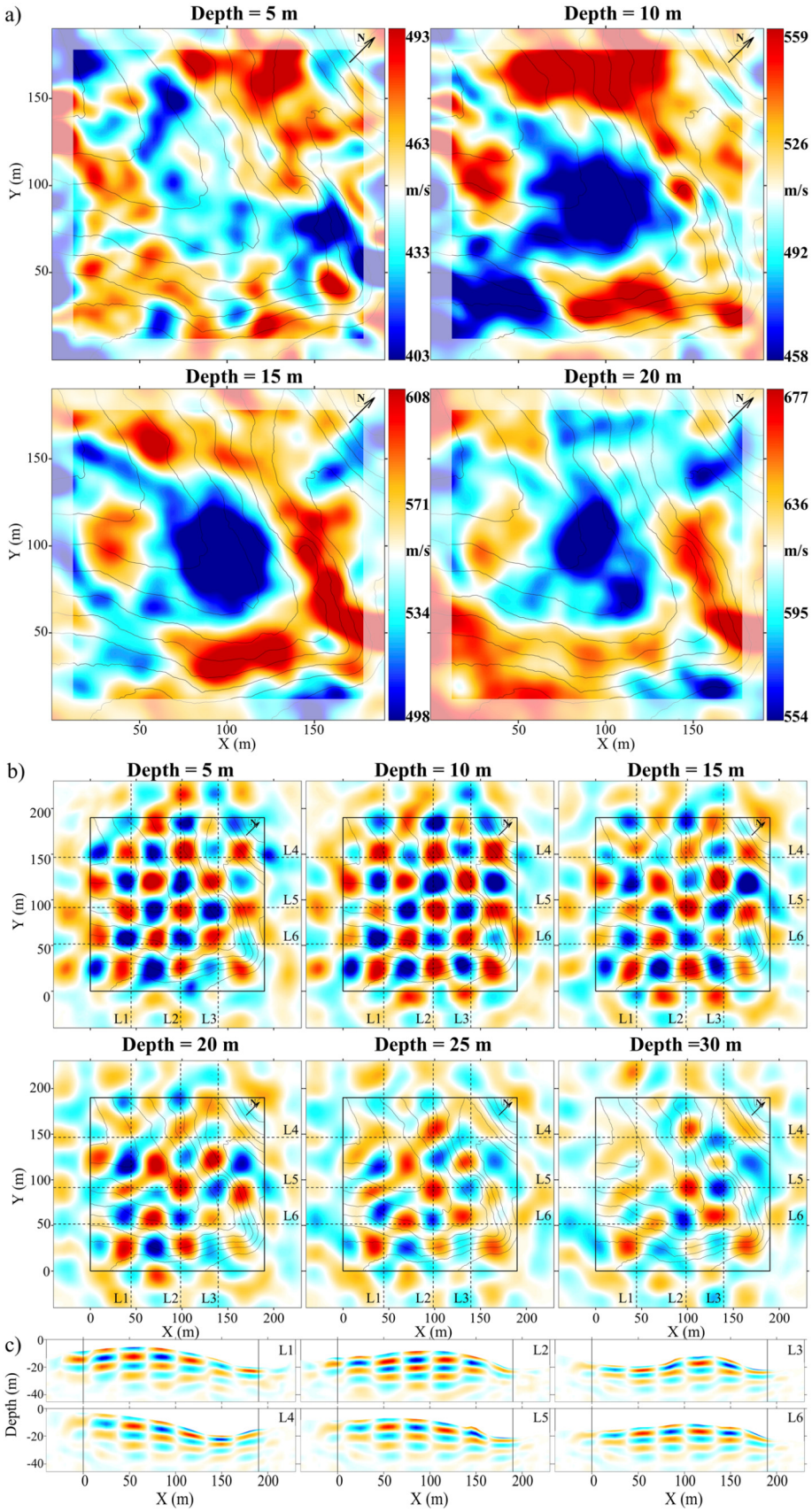


**Fig. 7.** a) Map-view plots of the 3D updated shear-wave velocity model at 5, 10, 15 and 20 m depth below the free surface. Warm colors: high shear-wave velocity; cold colors: low shear-wave velocity; white: the shear-wave velocity in the laterally homogenous starting model. Black arrow on upper-right corner of each plot shows direction of North. Gray contours show surface elevation; b) Map-view plots of checkerboard tests at 5, 10, 15, 20 m depth below the free surface. Black solid box is the dimension of our data array, black dash lines are locations of 6 cross sections as shown in Fig. 7c; c) Cross-section plots of checkerboard tests. Black vertical lines are the boundary of our data array. The vertical axis was exaggerated by 1.5 times.

exist in only minor volumes away from our study site (Edwards and Frost, 2000). Surface observations (Fig. 1b) and core samples extracted from boreholes (Flinchum et al., 2018) all suggest that our study site developed from relatively uniform Sherman Granite. The composition of the Sherman Granite has no substantial variations, with 30–40% microline, 15–30% of quartz, 20% plagioclase, 10–15% perthite and 5–10% biotite (Frost et al., 1999; Edwards and Frost, 2000).

### 5.2. Depth variations in shear-wave velocity

Lateral variations in shear-wave velocity observed in the constant-depth map-view plots (Fig. 7a) may reflect vertical variations of the transition between the saprolite of lower shear-wave velocity on the top and the fractured bedrock of higher shear-wave velocity below. The distinction between fractured bedrocks and saprolite is in the extent of chemical weathering. Core samples from boreholes and optical borehole images show that fractured bedrocks are characterized by extensive cracks due to physical weathering and the crack density decreases rapidly with depth from ∼8–12 fractures per meter at the top of the fracture bedrock to ∼1–3 fractures per meter near the top of pristine bedrock. Chemical weathering, in the form of stains, is confined to crack surfaces and the materials between cracks are largely intact fresh bedrocks. In contrast, saprolite materials obtained from augering samples have been chemically weathered thoroughly to the point of being friable (Flinchum et al., 2018).

Chemical weathering can increase porosity through mineral dissolution, thereby reducing shear-wave velocity (e.g., O'Connell and Budiansky, 1974). The increased porosity and surface areas of reacting minerals increase water-holding capacity of the regolith and promote water infiltration, which decreases concentration of soluble materials and leads to more weathering. Such a positive feedback between porosity creation and chemical weathering (e.g., Brantley et al., 2008) is exacerbated by biological activities (e.g., Banfield et al., 1999), which usually increase towards the surface. At our BW study site, the porosity measured from the borehole BWG6 near the center of our seismic array (Fig. 1a) increases from ∼0.34 at ∼9 m depth to ∼0.43 at ∼1 m depth, suggesting an acceleration of the positive feedback loop between chemical weathering and porosity creation towards the free surface.

The shear-wave velocity is less sensitive to the saturation of the porous material than the P-wave velocity, which is often imaged through conventional first-arrival refraction tomography. The volumetric water content measured from augering samples indicates that at the time of our seismic ambient-noise survey, the saprolite was mostly dry. First-order variations in the shear-wave velocity at our study site should therefore reflect major changes in porosity. To examine first-order variations of the shear-wave velocity with depth, we laterally averaged our updated 3D model and obtained the velocity-depth profile shown in Fig. 6c. The laterally averaged shear-wave velocity increases monotonically with depth and there exists an inflection zone between ∼9 m and ∼14 m depths. Fig. 6d shows the derivative of the laterally averaged shear-wave velocity with respect to depth and within this inflection zone the depth derivative is minimal.

We conjecture that the inflection zone on the laterally averaged velocity-depth profile (Fig. 6cd) marks the transition between highly chemically weathered saprolite and fractured bedrocks. Above this transition, average shear-wave velocity reduces towards the free surface at an increasing rate due to an acceleration of the positive feedback loop between porosity creation and chemical weathering. Below this transition, average shear-wave velocity increases with depth at an increasing rate because the fracture density reduces with depth at an increasing rate.

**Table 1**
Saprolite thickness at boreholes.

| Borehole name | Saprolite thickness (m) |
|---|---|
| BW1 | 14.98 |
| BW4 | 8.2 |
| BW6 | 15.61 |
| BW7 | 15.94 |
| BW8 | 14.88 |
| BW9 | 15.84 |
| BWG1 | 5.8 |
| BWG6 | 15.5 |
| BWG7 | 8.5 |

### 5.3. Weathering front

At our BW study site, the bottom of the saprolite marks the initiation of substantial chemical weathering and we use it for representing the weathering front in this study. The inflection zone on the laterally averaged velocity-depth profile suggests that the shear-wave velocity corresponding to the weathering front is likely to take upon any value between 450 m/s and 530 m/s. There are 9 boreholes, which consists of 6 bedrock boreholes (labeled BW in Fig. 1a) and 3 saprolite boreholes (labeled BWG in Fig. 1a) located inside our seismic array (Fig. 1a). We have saprolite depth (Table 1) for 3 saprolite boreholes and casing depth data for the 6 bedrock boreholes. The casing depth is the depth to which drillers inserted a large-diameter pipe to prevent upper friable materials from caving in and is ∼1.5 m below the transition from mechanically weak saprolite materials to more competent fractured bedrocks. For the saprolite boreholes, drillers provided depth data of the saprolite bottom inside the borehole. We can therefore use these borehole depth data to calibrate the shear-wave velocity corresponding to the weathering front.

Fig. 6b shows the histogram of the shear-wave velocity at the weathering front obtained from a bootstrap process of one million iterations. In each iteration of our bootstrap process, the bootstrap sample was taken randomly from the 9 original borehole depth data by using "sampling with replacement". And then we searched for the optimal shear-wave velocity between 450 m/s and 530 m/s such that its isosurface (represented as a depth value at every lateral grid position) in our updated 3D shear-wave velocity model has the smallest mismatch (defined in terms of the root-mean-square of the depth differences) with the depth data at the borehole locations in the bootstrap sample of that iteration. The histogram obtained from the bootstrap process can be fit with a normal distribution with mean ∼491 m/s and standard deviation 13.5 m/s (Fig. 6b). The isosurface of 491 m/s in our updated 3D shear-wave velocity model has a RMS mismatch of ∼3.2 m with the original borehole depth data.

The 491 m/s velocity contour has been highlighted on the two cross sections of our updated 3D shear-wave velocity model (Fig. 8ab) along the two lines A-A' and B-B' shown in Fig. 1a. On the cross sections, we also plotted the original borehole depth data, which are in general agreement with the 491 m/s contour. In areas with steep surface topography, the 491 m/s isosurface generally bends upward towards the free surface. Examples of this general observation can be seen on the two cross sections. On the along-ridge cross section (Fig. 8a) we see an upward bend of the 491 m/s contour underneath the eastern tip of the ridge between distance 190 and 230 m. On the cross-ridge cross section this upward bend is observed under both sides of the ridge between distance 70 and 80 m and between distance 160 and 180 m.

Our seismic data do not allow us to resolve the soil layer, which is very thin (less than ∼1 m) at our study site. We therefore grouped the soil layer with the saprolite layer in our analysis. The difference between the 491 m/s isosurface and the topographic el-

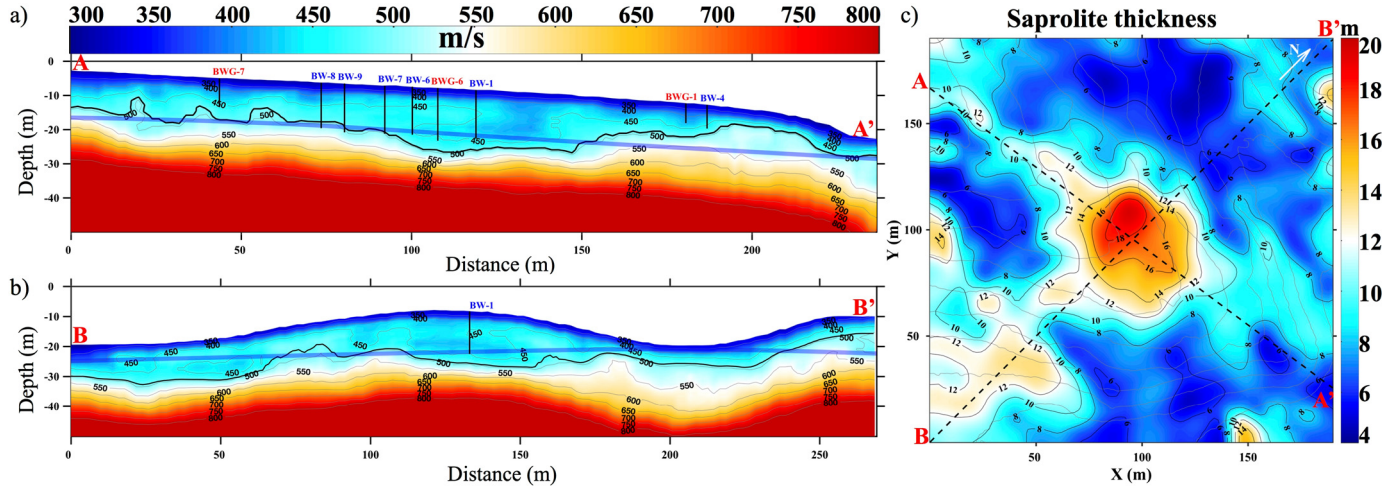


**Fig. 8.** a)–b) Cross sections of shear-wave velocity along A-A' and B-B' (Fig. 1a), vertical black bars: saprolite depth measurements obtained from boreholes, black lines: the 491 m/s contour line, thick blue lines: steady state groundwater table. c) Saprolite thickness map, white arrow on upper-right corner shows direction of North, gray contours show surface elevation, black contours show saprolite thickness, black dash lines are locations of two cross sections as shown in Fig. 8ab.

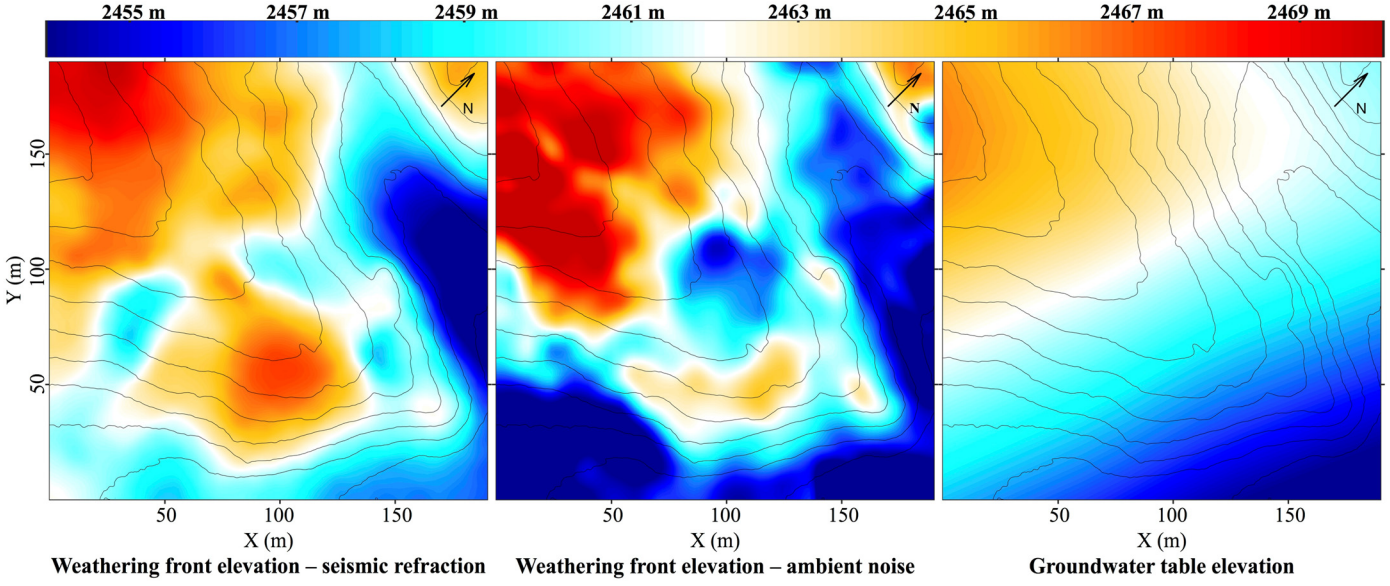


**Fig. 9.** a) Elevation of the 1200 m/s P-wave velocity isosurface obtained from seismic refraction study in Flinchum et al. (2018); b) elevation of the 491 m/s shear-wave velocity isosurface obtained from our full-3D ambient-noise tomography; c) elevation of steady state groundwater table. The black arrow on the upper-right corner of each plot shows direction of North. Gray contours show surface elevation.

evation of the free surface gives us an estimate of the saprolite thickness (Fig. 8c), which shows strong variations both across the ridge and along the ridge. In general, saprolite is thicker under the ridge and thinner under the valleys. Under the ridge, around the center of our model, the saprolite thickness reaches the maximum of ∼18 m, which is about twice as thick as other locations under the ridge. This area with the largest saprolite thickness is also clearly visible on the two cross sections (Fig. 8ab).

The weathering front, represented using the 491 m/s isosurface in our 3D shear-wave velocity model, is in general agreement with the 1200 m/s P-wave velocity isosurface used to represent the bottom of the saprolite in Flinchum et al. (2018) (Fig. 9ab). Within our study area, the correlation coefficient between these two isosurfaces is ∼0.76. The 1200 m/s P-wave velocity isosurface was obtained through interpolating 25 two-dimensional P-wave velocity refraction tomography results using ordinary kriging (Flinchum et al., 2018). Among the 25 refraction transects, two of them are located inside of our study area and three of them have significant portions lying inside our study area. The small-scale differences between the two surfaces shown in Fig. 9ab are mainly caused by differences in data coverage in the two studies.

Fig. 9c shows the steady state groundwater table elevation in our study area obtained by inverting water level measurements inside the 6 bedrock boreholes (Fig. 1a) and a hand-augered hole in the northern valley using the methods of Jiao and Zhang (2014). We assumed that the stream in the southern valley was connected to the groundwater in the inversion. A prediction of the "bottom-up", bedrock drainage model (Rempe and Dietrich, 2014) is that the weathering front should locate approximately around the groundwater table. The eastward gradient of the inverted groundwater table (Fig. 9c) is in broad agreement with the overall eastward slope observed in the weathering fronts obtained from seismic tomography (Fig. 9ab). The correlation coefficient between the 491 m/s shear-wave velocity isosurface and the groundwater table is ∼0.74. However, the inverted groundwater table does not show small-scale cross-ridge and along-ridge variations that exist in the two isosurfaces obtained from seismic tomography (Fig. 9ab).

The cross-ridge variations in saprolite thickness (Fig. 8c) can potentially be explained using "top-down" mechanisms (Lebedeva and Brantley, 2013). In particular, as the topographic surface gradually steepens downslope, the slope-normal component of the vertical water flux reduces progressively, which may lead to downslope thinning of the saprolite layer. However, this geometric mechanism alone may not be sufficient to explain the along-ridge variations in saprolite thickness shown in Fig. 8c. Recent models of "top-down" processes have taken into account influences of pre-existing fractures, showing that fractures and joints inherited from parent bedrocks can facilitate downward infiltration of meteoric water, which may potentially produce spatially localized thick weathered zones (Reis and Brantley, 2017). Recent seismic surveys using "circle shots" in the BW area have detected shallow seismic anisotropy in saprolite that may come from lithic fabrics of pre-existing fractures and the amount of anisotropy is correlated with saprolite thickness (Novitsky et al., 2018).

## 6. Conclusion

Seismic tomography is becoming an increasingly important tool for studying the structures and processes inside the CZ (Parsekian et al., 2015). In this study, we have successfully applied full-3D adjoint tomography to seismic ambient-noise data collected through a high-density "large-N" seismic survey to image CZ structure under a granite ridge in the BW watershed. The 3D seismic shear-wave velocity model obtained after 5 adjoint iterations has revealed strong lateral heterogeneities, which are correlated with surface topography, and depth variations, which might be indicative of the degree of subsurface chemical weathering.

By examining the velocity-depth profile obtained through lateral averaging of our 3D model, we identified a possible range of shear-wave velocities for representing the bottom of the saprolite layer. Further calibration using borehole saprolite depth measurements showed that the isosurface of shear-wave velocity 491 m/s likely marks the bottom of saprolite, which we use as the weathering front in this study.

The weathering front obtained from our 3D shear-wave velocity model is highly consistent with the saprolite-bedrock interface obtained from an independent P-wave velocity seismic refraction tomography study (Flinchum et al., 2018). It also shows large-scale consistency with the groundwater table obtained by inverting water level observations in boreholes.

There also exist substantial discrepancies between the weathering front determined through seismic tomography and the inverted groundwater table, especially at smaller spatial scales. Such discrepancies cannot be easily explained using the highly simplified model of Rempe and Dietrich (2014), which builds upon a topography-driven groundwater flow model. The ground-water system, as observed at Blair Wallis, suggests the existence of a local, km-scale groundwater flow system that is likely topography driven. However, the factors that control water table depth/variation are more complex than the influence of topography alone. It is generally accepted that groundwater table is controlled by the interplay of 3 factors: subsurface permeability (i.e., lithology and/or fractures), climate (i.e., recharge rate), and topography. Such interplay often results in a groundwater table not reflecting topographical variation (Condon and Maxwell, 2015, and citations therein). Moreover, over the time scale controlling landscape evolution, erosion, besides changing the topographic gradient, and therefore one of the factors influencing the water table configuration, will likely increase the permeability of the subsurface. This increasing permeability will likely exert a negative feedback via a deepening of the water table, thus a de-coupling from the near-surface mechanisms described in the "bottom-up" hypothesis in Rempe and Dietrich (2014), where water table must intersect streams. In addition, climate change over the same (landscape evolution) time scale will likely include dry and wet periods: only a wet climate, along with a relatively low subsurface permeability (K), promotes a shallow water table that intersects streams that is required by the bottom-up hypothesis. In a dry climate, water table most likely lies deep and thus has limited interaction with surface water.

To fully explain the spatial variations in our weathering front, we may require both the "bottom-up" and "top-down" mechanisms. In particular, small-scale spatial variations in our weathering front may require explanations of "top-down" processes that account for the influences of pre-existing fractures (Reis and Brantley, 2017).

## Acknowledgements

Financial support for Wei Wang was partially provided by National Science Foundation Grant EPS-1208909 to Wyoming Center for Environmental Hydrology and Geophysics. We thank Brady Flinchum for sharing his seismic refraction results. We thank the NCAR-Wyoming Supercomputing Center (NWSC) for providing the computational resources used in this study. Comments from editor Jean-Philippe Avouac and an anonymous reviewer improved the manuscript.

## References

Anderson, S.P., von Blanckenburg, F., White, A.F., 2007. Physical and chemical controls on the critical zone. Elements 3 (5), 315–319.

Banfield, J.F., Barker, W.W., Welch, S.A., Taunton, A., 1999. Biological impact on mineral dissolution: application of the lichen model to understanding mineral weathering in the rhizosphere. Proc. Natl. Acad. Sci. 96 (7), 3404–3411.

Befus, K.M., Sheehan, A.F., Leopold, M., Anderson, S.P., Anderson, R.S., 2011. Seismic constraints on critical zone architecture, Boulder Creek watershed, Front Range, Colorado. Vadose Zone J. 10 (4), 1342. https://doi.org/10.2136/vzj2010.0108er.

Bensen, G.D., Ritzwoller, M.H., Barmin, M.P., Levshin, A.L., Lin, F., Moschetti, M.P., Shapiro, N.M., Yang, Y., 2007. Processing seismic ambient noise data to obtain reliable broad-band surface wave dispersion measurements. Geophys. J. Int. 169 (3), 1239–1260.

Brantley, S.L., White, T.S., White, A.F., Sparks, D., Richter, D., Pregitzer, K., Derry, L., Chorover, J., Chadwick, O., April, R., Anderson, S., Amundson, R., 2006. Frontiers in Exploration of the Critical Zone. An NSF-sponsored Workshop. National Science Foundation, 30 pp.

Brantley, S.L., Bandstra, J., Moore, J., White, A.F., 2008. Modelling chemical depletion profiles in regolith. Geoderma 145, 494–504.

Carey, A.M., Paige, G.B., 2016. Ecological site-scale hydrologic response in a semiarid rangeland watershed. Rangeland Ecol. Manag. 69 (6), 481–490.

Chapin, C.E., Kelley, S.A., 1997. The Rocky Mountain erosion surface in the Front Range of Colorado.

Chen, M., Huang, H., Yao, H., van der Hilst, R., Niu, F., 2014. Low wave speed zones in the crust beneath SE Tibet revealed by ambient noise adjoint tomography. Geophys. Res. Lett. 41, 334–340.

Chen, P., Zhao, L., Jordan, T.H., 2007. Full 3D tomography for the crustal structure of the Los Angeles region. Bull. Seismol. Soc. Am. 97 (4), 1094–1120. https://doi.org/10.1785/0120060222.

Chen, P., Lee, E.J., 2015. Full-3D Seismic Waveform Inversion: Theory, Software and Practice. Springer.

Chen, P., Taylor, N.J., Dueker, K.G., Keifer, I.S., Wilson, A.K., McGuffy, C.L., Novitsky, C.G., Spears, A.J., Holbrook, W.S., 2016. pSIN: a scalable, parallel algorithm for seismic interferometry of large-N ambient-noise data. Comput. Geosci. 93, 88–95. https://doi.org/10.1016/j.cageo.2016.05.003.

Condon, L.E., Maxwell, R.M., 2015. Evaluating the relationship between topography and groundwater using outputs from a continental scale integrated hydrology model. Water Resour. Res. 51. https://doi.org/10.1002/2014WR016774.

Dethier, D.P., Ouimet, W., Bierman, P.R., Rood, D.H., Balco, G., 2014. Basins and bedrock: spatial variation in 10Be erosion rates and increasing relief in the southern Rocky Mountains, USA. Geology 42 (2), 167–170.

Dumbser, M., Käser, M., 2006. An arbitrary high order discontinuous Galerkin method for elastic waves on unstructured meshes II: the three-dimensional isotropic case. Geophys. J. Int. 167 (1), 319–336. https://doi.org/10.1111/j.1365-246X.2006.03120.x.

Edwards, B.R., Frost, C.D., 2000. An overview of the petrology and geochemistry of the Sherman batholith, southeastern Wyoming: identifying multiple sources of Mesoproterozoic magmatism. Rocky Mt. Geol. 35 (1), 113–137.

Eggler, D.H., Larson, E.E., Bradley, W.C., 1969. Granites, grusses, and the Sherman erosion surface, southern Laramie Range, Colorado-Wyoming. Am. J. Sci. 267 (4), 510–522.

Fichtner, A., 2011. Full Seismic Waveform Modelling and Inversion. Springer, Berlin/Heidelberg.

Flinchum, B.A., Steven Holbrook, W., Rempe, D., Moon, S., Riebe, C.S., Carr, B.J., et al., 2018. Critical zone structure under a granite ridge inferred from drilling and three-dimensional seismic refraction data. J. Geophys. Res., Earth Surf. 123, 1317–1343. https://doi.org/10.1029/2017JF004280.

Frost, C.D., Frost, B.R., Chamberlain, K.R., Edwards, B.R., 1999. Petrogenesis of the 1.43 Ga Sherman batholith, SE Wyoming, USA: a reduced, rapakivi-type anorogenic granite. J. Petrol. 40 (12), 1771–1802.

Gao, H., Shen, Y., 2014. Upper mantle structure of the cascades from full-wave ambient noise tomography: evidence for 3D mantle upwelling in the back-arc. Earth Planet. Sci. Lett. 309, 222–233.

Holbrook, W.S., Riebe, C.S., Elwaseif, M., Hayes, J.L., Basler-Reeder, K., Harry Malazian, D.L., Dosseto, A., Hartsough, P.C., Hopmans, J.W., 2014. Geophysical constraints on deep weathering and water storage potential in the Southern Sierra Critical Zone Observatory. Earth Surf. Process. Landf. 39 (3), 366–380. https://doi.org/10.1002/esp.3502.

Holschneider, M., Diallo, M.S., Kulesh, M., Ohrnberger, M., Lück, E., Scherbaum, F., 2005. Characterization of dispersive surface waves using continuous wavelet transforms. Geophys. J. Int. 163 (2), 463–478.

Hunter, J.A., Pullan, S.E., Burns, R.A., Gagne, R.M., Good, R.L., 1984. Shallow seismic reflection mapping of the overburden–bedrock interface with the engineering seismograph—some simple techniques. Geophysics 49, 1381–1385. https://doi.org/10.1190/1.1441766.

Jiao, J., Zhang, Y., 2014. Two-dimensional physical-based inversion of confined and unconfined aquifers under unknown boundary conditions. Adv. Water Resour. 65, 43–57.

Käser, M., Castro, C., Hermann, V., Pelties, C., 2010. SeisSol – a software for seismic wave propagation simulations. In: High Performance Computing in Science and Engineering. Garching/Munich 2009. Springer, Berlin, Heidelberg, pp. 281–292.

Käser, M., Dumbser, M., 2006. An arbitrary high order discontinuous Galerkin method for elastic waves on unstructured meshes I: the two-dimensional isotropic case with external source terms. Geophys. J. Int. 166 (2), 855–877. https://doi.org/10.1111/j.1365-246X.2006.03051.x.

Keifer, I., Dueker, K., under review. Ambient Rayleigh wave field imaging of the critical zone in a weathered granite terrane. Earth Planet. Sci. Lett.

Kulesh, M., Holschneider, M., Diallo, M.S., 2008. Geophysical wavelet library: applications of the continuous wavelet transform to the polarization and dispersion analysis of signals. Comput. Geosci. 34 (12), 1732–1752.

Lebedeva, M.I., Brantley, S.L., 2013. Exploring geochemical controls on weathering and erosion of convex hillslopes: beyond the empirical regolith production function. Earth Surf. Process. Landf. 38 (15), 1793–1807.

Lee, E.J., Chen, P., Jordan, T.H., Maechling, P.B., Denolle, M.A., Beroza, G.C., 2014. Full-3-D tomography for crustal structure in southern California based on the scattering-integral and the adjoint-wavefield methods. J. Geophys. Res., Solid Earth 119 (8), 6421–6451.

Lee, E.-J., Chen, P., 2013. Automating seismic waveform analysis for full 3-D waveform inversions. Geophys. J. Int. 194 (1), 572–589. https://doi.org/10.1093/gji/ggt124.

Lin, F.C., Moschetti, M.P., Ritzwoller, M.H., 2008. Surface wave tomography of the western United States from ambient seismic noise: Rayleigh and Love wave phase velocity maps. Geophys. J. Int. 173 (1), 281–298.

Lowry, M.E., Crist, M.A., Tilstra, J.R., 1967. Geology and Ground-Water Resources of Laramie County, Wyoming; with a Section on Chemical Quality of Ground Water and of Surface Water. No. 1834. US Govt. Print. Off.

Merrill, G.P., 1897. A Treatise on Rocks, Rock-Weathering and Soils. Macmillan Company, New York.

Novitsky, C.G., Steven Holbrook, W., Carr, B.J., Pasquet, S., Okaya, D., Flinchum, B.A., 2018. Mapping inherited fractures in the critical zone using seismic anisotropy from circular surveys. Geophys. Res. Lett..

NRC (National Research Council), 2001. Basic Research Opportunities in Earth Science. National Academy Press, Washington. 154 pp.

NRCS (Natural Resources Conservation Service), 2015. Crow Creek SNOTEL site. United States Department of Agriculture. SNOTEL surveys. Available online at http://wcc.sc.egov.usda.gov/nwcc/site?sitenum=1045. (Accessed 15 July 2017).

O'Connell, R.J., Budiansky, B., 1974. Seismic velocities in dry and saturated cracked solids. J. Geophys. Res. 79, 5412–5426.

Parsekian, A.D., Singha, K., Minsley, B.J., Holbrook, W.S., Slater, L., 2015. Multiscale geophysical imaging of the critical zone. Rev. Geophys. 53 (1), 1–26.

Press, W.H., Teukolsky, S.A., Vetterling, W.T., Flannery, B.P., 1992. Numerical Recipes in C, the Art of Scientific Computing. Cambridge Univ. Press, New York.

Rempe, D.M., Dietrich, W.E., 2014. A bottom-up control on fresh-bedrock topography under landscapes. Proc. Natl. Acad. Sci. 111 (18), 6576–6581.

Reis, F.D., Brantley, S.L., 2017. Models of transport and reaction describing weathering of fractured rock with mobile and immobile water. J. Geophys. Res., Earth Surf. 122 (3), 735–757.

Shapiro, N.M., Campillo, M., Stehly, L., Ritzwoller, M.H., 2005. High-resolution surface-wave tomography from ambient seismic noise. Science 307 (5715), 1615–1618.

Stolt, M.H., Baker, J.C., 1994. Strategies for studying saprolite and saprolite genesis. In: Whole Regolith Pedology, pp. 1–19.

Tape, C., Liu, Q., Maggi, A., Tromp, J., 2009. Adjoint tomography of the southern California crust. Science 325 (5943), 988–992. https://doi.org/10.1126/science.1175298.

Tarantola, A., 1988. Theoretical background for the inversion of seismic waveforms including elasticity and attenuation. Pure Appl. Geophys. 128 (1–2), 365–399. https://doi.org/10.1007/BF01772605.

Tromp, J., Tape, C., Liu, Q., 2005. Seismic tomography, adjoint methods, time reversal and banana-doughnut kernels. Geophys. J. Int. 160 (1), 195–216. https://doi.org/10.1111/j.1365-246X.2004.02453.x.

Wald, D.J., Allen, T.I., 2007. Topographic slope as a proxy for seismic site conditions and amplification. Bull. Seismol. Soc. Am. 97, 1379–1395.

Zhao, L., Jordan, T.H., Olsen, K.B., Chen, P., 2005. Fréchet kernels for imaging regional Earth structure based on three-dimensional reference models. Bull. Seismol. Soc. Am. 95 (6), 2066–2080.